13

3D Simulation of Normal and Oblique Penetration and Perforation

13.1 Introduction

The 2D simulation of normal penetration has been described in Chapter 12. The same problem is re-investigated through 3D simulation using the model proposed by Zhou at Nanyang Technological University (NTU), Singapore, which is the combination of the unified strength theory (Yu, 1998; 2004) and the experimental data.

The 3D simulation of oblique penetration and the perforation process through a concrete slab was also simulated by Zhou XQ at NTU, Singapore in 2002. The unified strength theory with parameter b=0.6 (Fig. 12.3) is implemented in AutDYN (2000) and used again for simulation of the penetration problem.

13.2 Simulation of Normal Impact Process

In this section,the same problem in section 12.3 is investigated through 3D simulation using the present model. Figure 13.1 shows the 3D finite element mesh used in the numerical model. In Fig. 13.1, three front layers of concrete elements are removed to show the reinforcement grid. The structure is modeled by 48×48×14 brick concrete elements and 3 layers of 8×8 beam reinforcement elements.

This chapter is contributed by Prof. Zhou XQ

M.-H. Yu et al., *Computational Plasticity*

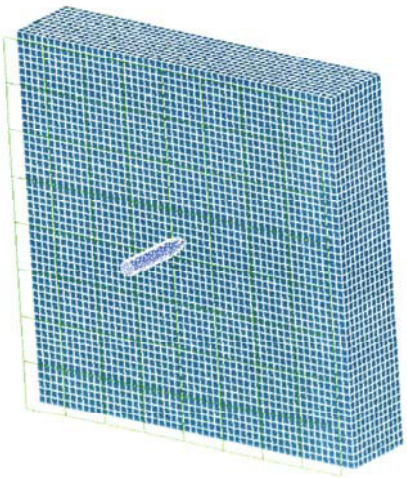

Fig. 13.1 The FE-mesh used in the 3D numerical simulation (Zhou, 2002)

The results of simulation using the UST with b=0.6 are obtained. The material status at different time cycles is shown in Figs. 13.2 to 13.8 (Zhou, 2002).

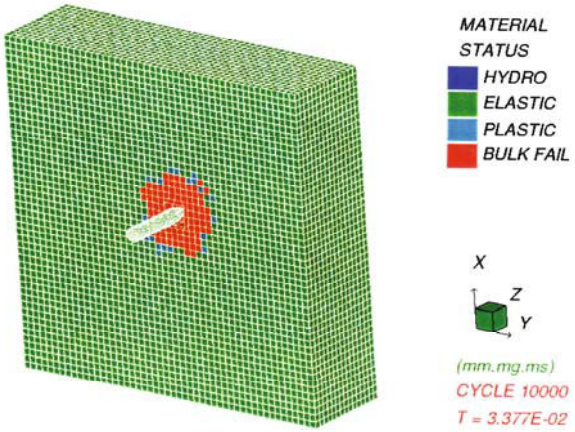

Fig. 13.2 Material status at cycle 10000 (Zhou, 2002)

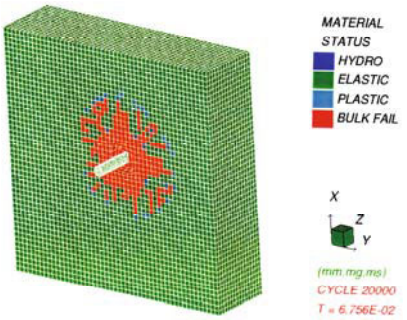

Fig. 13.3 Material status at cycle 20000

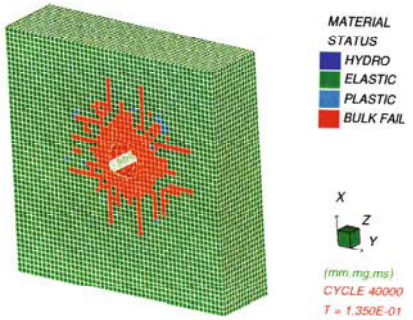

Fig. 13.4 Material status at cycle 40000

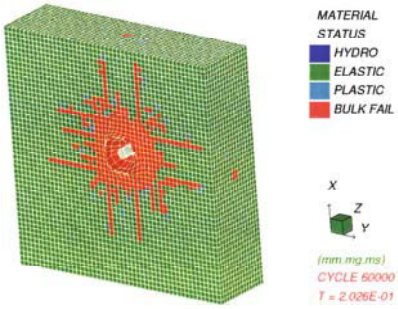

Fig. 13.5 Material status at cycle 60000

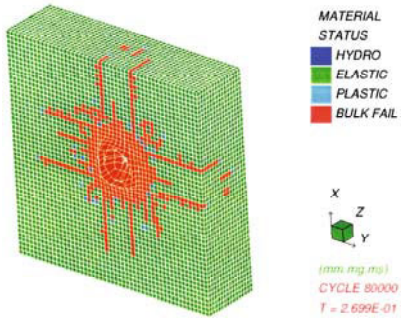

Fig. 13.6 Material status at cycle 80000

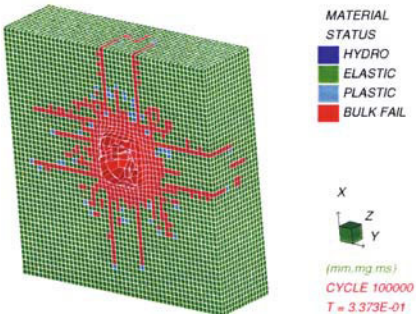

Fig. 13.7 Material status at cycle 100000 (impact surface)

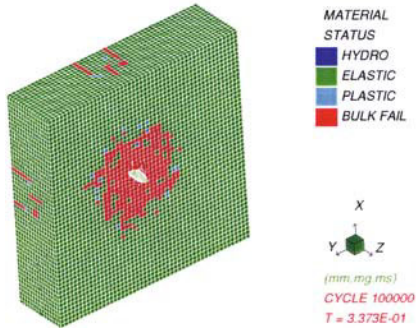

Fig. 13.8 Material status at cycle 100000 (exit surface)

Figures 13.9 and 13.10 reproduce Hanchak's post-test photographs revealing the damage to the front (impact) surface and the rear (exit) surface respectively. By comparing the size of the damaged areas shown in Figs. 13.9 and 13.10 with those in the post-test photographs in Figs. 13.9 and 13.10, the following can be seen.

(1) On the impact surface, the size of the damaged crater obtained by numerical simulation agrees fairly well with that shown in the post-test

photograph (see Figs. 13.7 and 13.9a);

(2) On the exit surface, the size of the damaged crater obtained from numerical simulation is slightly smaller than that shown in the post-test photograph (see Figs. 13.8 and 13.9b).

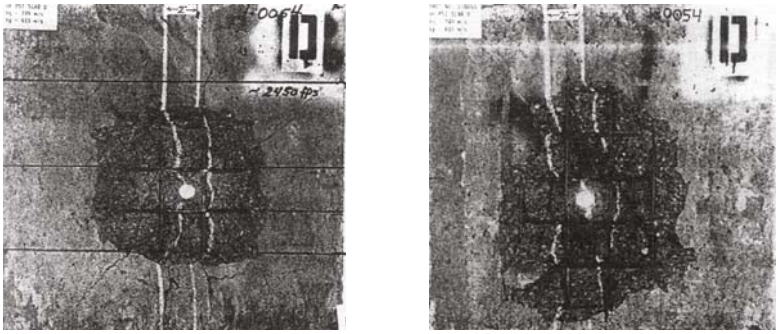

(a) Impact surface (b) Rear surface

Fig. 13.9 Post-test photograph

The velocity history of the projectile is shown in Fig. 13.10. It can be observed that the exit velocity is about 575 m/s, which is about 5%-6% lower than the experimental result of 610 m/s. Against this background, an alternate 3D simulation with reinforcement omitted was carried out, and the exit velocity becomes 625 m/s (2%-3%higher than 610 m/s). It suggests that the strengthening effect derived from the steel reinforcement bars is over-estimated. This is due to the assumption of perfect bonding between the steel bars and their surrounding concrete (even though they are only pin-jointed at the nodes). However, it shows that the effect of reinforcement bars is minimal.

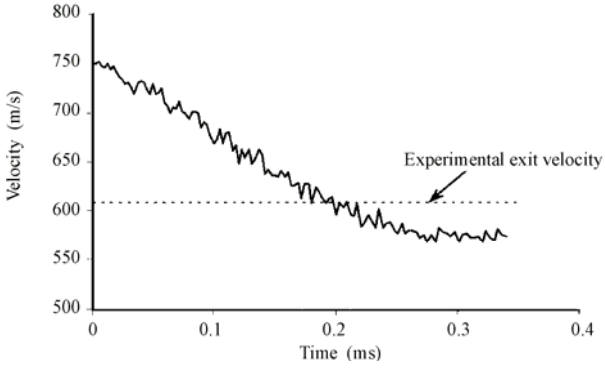

Fig. 13.10 Velocity history of projectile

13.3 Simulation of Oblique Impact Process

The oblique perforation process through a concrete slab has to be a 3D simulation. The impact configurations match those in the experimental tests carried out by Buzaud et al. (1999) in France. The concrete slab is 3000 mm square and has a thickness of 600 mm. The high-strength steel projectile hits the center of the slab at a velocity of 338 m/s with a 30° angle of incidence (measured in the horizontal plane) and a 0° angle of attack (measured in the vertical plane).

Figure 13.11 shows the geometric configurations of the projectile. The projectile was machined out of a 35NCDl6 high strength steel rod with an elasticity limit of l300 MPa. Having a total length of 960 mm and a diameter of l60 mm, its nose is tangent ogive shape with a Caliber Radius Head (CRH) of 6. The thickness of the afterbody is between 17 and 20 mm.

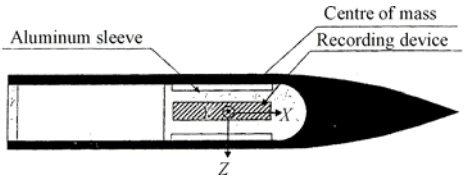

Fig. 13.11 Geometry of the steel projectile

The geometric configuration of the reinforced concrete target is shown in Fig. 13.12. The target is reinforced by a layer of ϕ16 mm high-adherence steel bars at a

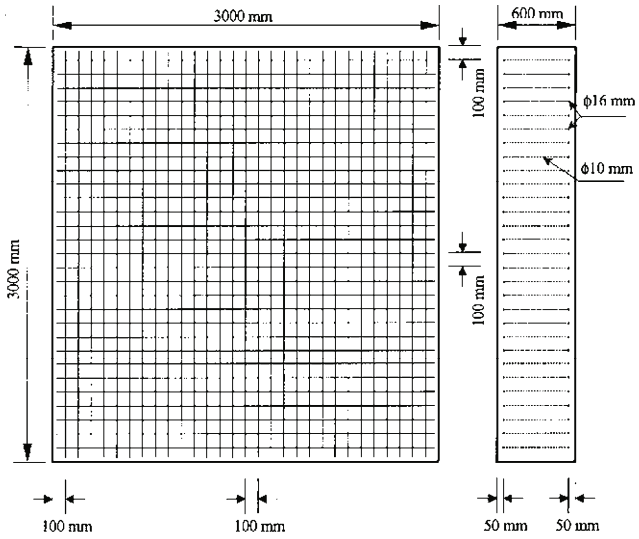

Fig. 13.12 Configuration of concrete target (Zhou, 2002)

distance of 50 mm from the front and another layer at the rear face. The spacing between the ϕ16 mm bars is l00 mm in both directions. The two meshes are bound together by ϕ10 mm high-adherence stirrups at each node. The steel-to-concrete area ratio is 0.67%, which is regarded as light reinforcement to the concrete slab. Against this background, as guided by the experience of previous simulations, the reinforcement bars are not included in the simulation.

Tables 13.1 and 13.2 give the material constants for the concrete. The erosion limit for the incremental geometric strain is set at 150%. It is worth noting that a smaller erosion limit is necessary in 3D simulation. Otherwise, a numerical stability problem may occur and the computation process may stall due to excessive element distortion.

Table 13.1 General material parameters for concrete target

Parameter	Value	Parameter	Value
Reference density	2454.2 kg/m^3	Shear modulus	8.4 GPa
Solid sound speed	2693.17 m/s	Porous sound speed	2693.17 m/s
Compressive strength	43 MPa	H_t'	15 GPa
Tensile strength	4.0 MPa	E	20 GPa
Parameter of the UST, b	0.6	D_1	0.03
K_{co}	0.5	D_2	1.0
K_{t0}	0.9	P_{lo}	40 MPa
H_t'	15 GPa	P_{uo}	55 MPa

Table 13.2 Piece-wise linear porous EOS (pressure versus density)

Density (kg/m^3)	Pressure (MPa)
2368	0
2378	44
2411	180
2446.5	333

Figure 13.13 shows the finite element mesh for the projectile and the target. Figures 13.14–13.21 show the material status at different time cycles (Zhou, 2002).

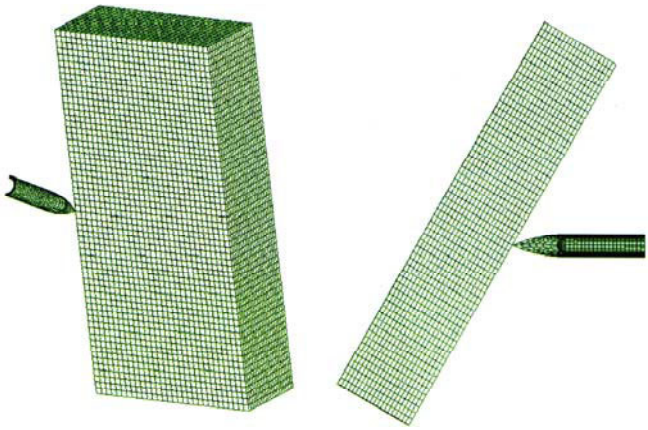

Fig. 13.13 The finite element mesh used in the numerical simulation (Zhou, 2002)

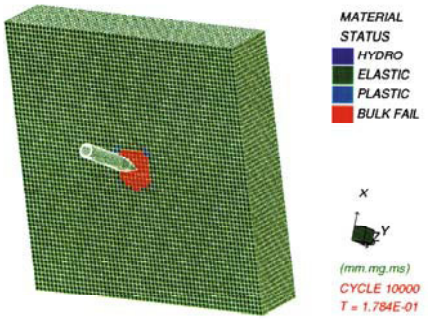

Fig. 13.14 Material status at cycle 10000

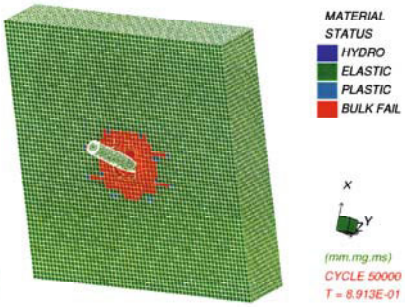

Fig. 13.15 Material status at cycle 50000

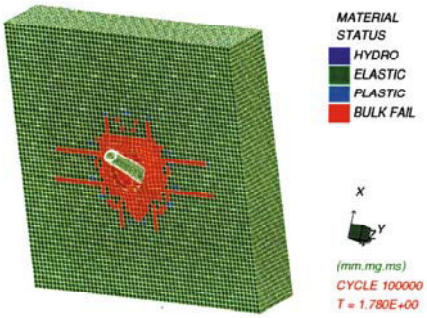

Fig. 13.16 Material status at cycle 100000

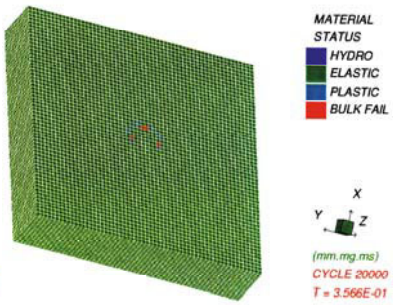

Fig. 13.17 Material status at cycle 20000 (rear surface view)

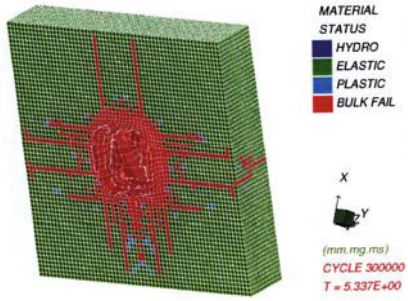

Fig. 13.18 Material status at cycle 30000

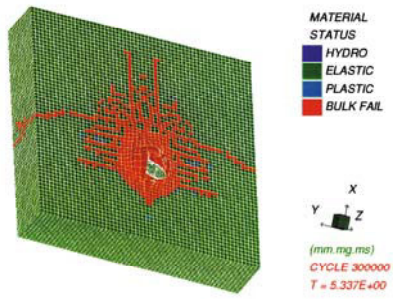

Fig. 13.19 Material status at cycle 300000 (rear surface view)

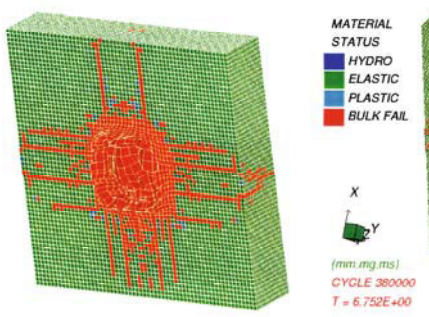

Fig. 13.20 Material status at cycle 380000

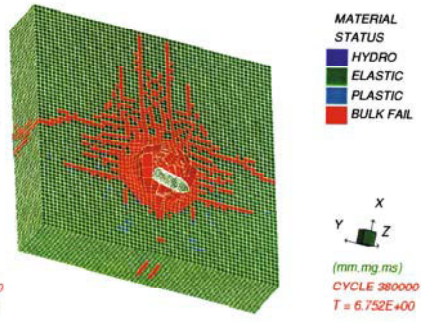

Fig. 13.21 Material status at cycle 380000 (rear surface view)

Figures 13.22 and 13.23 show the experimental results of the residual damaged area appearing on the front and rear face respectively. With regard to the size of the damaged areas on the front (Fig. 13.20) and rear face (Fig. 13.21), comparisons show that the simulation results agree well with the experimental ones (Figs. 13.22 and 13.23). With regard to the initiation point of damage on the rear face and the exit point from the rear face, simulation results (Fig. 13.20 and 13.21), comparisons also show a good accord between the numerical simulation and the experimental results (Fig. 13.23).

The projectile's exit-velocity history is shown in Fig. 13.24. It can be seen that the exit velocity is about 214 m/s, which is slightly higher (~l8%) than the experimental result of l80 m/s. It could be partly due to the omission of steel reinforcement bars in the numerical simulation. On the other hand, the pre-defined erosion limit is set lower than 2, which leads to a softer target material and results in a higher exit velocity.

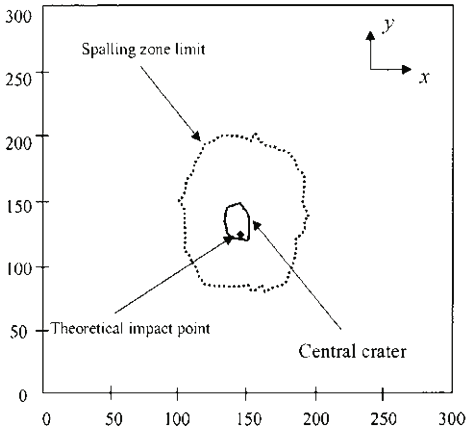

Fig. 13.22 Target residual damage (front face)

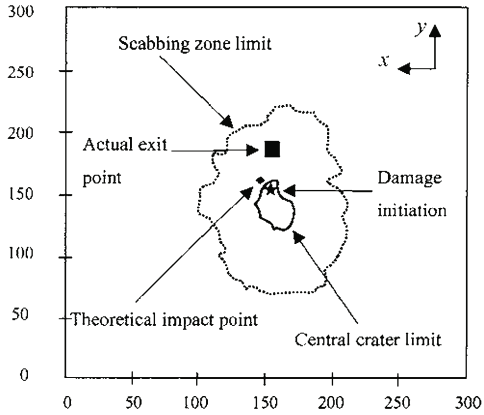

Fig. 13.23 Target residual damage (rear face)

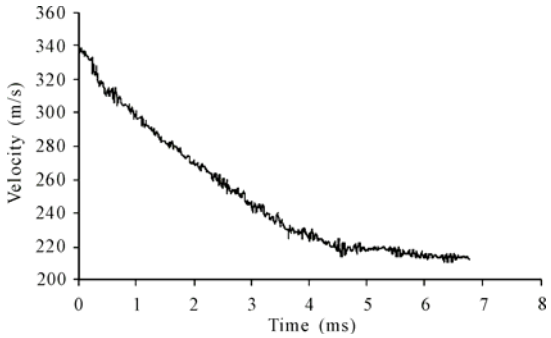

Fig. 13.24 Velocity history of the projectile

13.4 Conclusions

The following conclusions were given by Zhou.

1) Regarding the construction of the strength surface for the failure state of concrete material under triaxial stress condition, most of the available models are empirical criteria based on limited experimental data, such as the Willam-Wamke criterion, Ottosen criterion and Kotsovos-Palovic model (see: Chapter 3). On the other hand, Yu's Unified Twin Shear Stress (UTSS) theory offers a more thorough theoretical insight into the strength criteria. The UTSS clearly defined the role of the intermediate principle shear stress through a contribution factor 'b' ($0 \leq b \leq 1$). Though the UTSS does not provide a complete theoretical strength criterion in the tri-axial stress space (π-space), it is proven to be logical and accurate in the π-space. Against this background, the present study leads to a novel way of constructing the strength surface—a semi-theoretical semi-empirical envelope. Subsequently, it is further developed into a multi-surface strength model for concrete materials. It takes into account the pre-failure elasto-plastic behavior and the post failure damages.

2) The development of the present model evolves from a static version SMl, which follows Yu's UTSS conical failure envelope. An improved static version SMII incorporates Yu's twin-shear criterion in the π-plane with Kotsovos' meridians. The dynamic version is a further development of SMII including the dynamic effects.

3) Construction of the failure envelope in the π-space is the key step. Rules governing the non-linear responses of concrete at different stress stages can be established. The rules for pre-failure behavior follow the elastic-plastic theory, while damage mechanics can be employed to govern the post-failure responses to account for the degradation of both strength and stiffness. The stress states at different stages of the stress path are described with respect to the failure surface. Other surfaces are thus derived to further partition the π-space into sub-zones. The partitioning surfaces demarcate the elastic zone, plastic zone and damage zone.

4) Both static models (UTSS-based SMI and semi-UTSS SMII) can yield reasonably accurate predictions for the ultimate capacity and the overall load-deflection response of RC beams (see Chapter 11). Model SMI leads to results inferior to those from model SMII. In particular, model SMII shows its robustness in the benchmark test for a box beam (see Chapter 11).

5) The dynamic version of the present MSS model, together with other available numerical techniques, are capable of simulating the complicated penetration and perforation process. Not only the velocity history of the projectile, but also the damage zones and the overall performance can be obtained with an acceptable degree of accuracy.

References

AutoDYN (2000) Theory Manual. Century Dynamics Inc.

Buzaud E, Laurenson R, Darrigade A et al. (1999) Hard target defeat: An analysis of reinforced concrete perforation process. The Ninth Int. Symp. on Interaction of the Effects of Munitions with Structures, Berlin, Germany, 3-7 May, 283-290.

Yu MH (1998) Twin Shear Theory and its Applications. Science Press: Beijing in Chinese).

Yu MH (2004) Unified Strength Theory and its Applications. Springer: Berlin.

Zhou XQ (2002) Numerical Analysis of Reinforcement Concrete Using Multi-Surface Strength Model. Doctoral Thesis at Nanyang Technological University, Singapore.